

Exchange effects in spin polarized transport through carbon nanotube quantum dots

Christoph Schenke, Sonja Koller, Leonhard Mayrhofer, and Milena Grifoni
Institut für Theoretische Physik, Universität Regensburg, 93035 Regensburg, Germany
 (Dated: March 29, 2010)

We investigate linear and nonlinear transport across single-walled carbon nanotube quantum dots weakly coupled to spin-polarized leads. We consider metallic tubes of finite length and small diameter, where not only forward scattering contributions of the Coulomb potential, but also short-ranged processes play an important role. In particular, they induce exchange effects leading for electron fillings $4n+2$ either to a non-degenerate groundstate of spin $S = 0$ or to a triplet groundstate. In the linear regime we present analytical results for the conductance - for both the $S = 0$ and the triplet groundstate - and demonstrate that an external magnetic field is crucial to reveal the spin nature of the groundstates. In the nonlinear regime we show stability diagrams that clearly distinguish between the different groundstates. We observe a negative differential conductance (NDC) effect in the $S = 0$ groundstate for antiparallel lead magnetization. In presence of an external magnetic field, spin blockade effects can be detected, again leading to NDC effects for both groundstates.

PACS numbers: 73.63.Fg, 72.25.-b, 73.23.Hk, 85.75.-d

I. INTRODUCTION

Since their discovery by S. Iijima and T. Ichihashi¹ in 1993, single-walled carbon nanotubes (SWNTs) have attracted attention due to their remarkable electronic and mechanical properties^{2,3}. At low energies, they represent an almost perfect realization of a one-dimensional (1D) system of interacting electrons with an additional orbital degree of freedom due to the sublattice structure of graphene. Accounting for spin and orbital degrees of freedom implies that for nanotubes a shell structure is expected, where each shell can accommodate up to four electrons. In the absence of Coulomb interaction the energy levels are spin degenerate, while the orbital degeneracy is usually lifted due to the nanotube finite length. Coulomb interactions, however, modify this picture. The sublattice structure of graphene gives rise to a distinction between electron interactions on the same and on different sublattices. Therefore, besides the long-ranged forward scattering processes, also short-ranged interaction processes play a role in small diameter tubes⁴⁻⁷. These short-ranged interactions cause in finite size nanotubes exchange effects leading for a tube filling of $4n + 2$ to a groundstate with either total spin $S = 0$ or $S = \hbar$ (a triplet)⁷. Signatures of the exchange interactions have indeed been inferred from stability diagrams of carbon-nanotube-based quantum dots⁸⁻¹⁰. In particular it was shown by Moriyama et al.⁸ that an applied magnetic field can be used to reversibly change the groundstate from the singlet to one of the triplet states.

Recently, carbon nanotubes have also attracted much attention for their potential applications in spintronic devices¹¹. They are particularly interesting because they have a long spin lifetime and can be contacted with ferromagnetic materials. Indeed, spin-dependent transport in carbon nanotube spin valves has been demonstrated by various experimental groups¹²⁻¹⁴, ranging from the Fabry-Perot^{12,13} to the Kondo regime¹⁴.

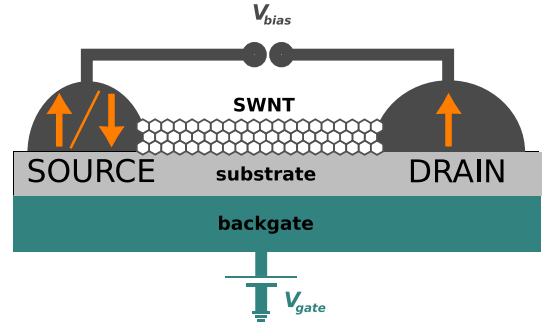


FIG. 1: Single-electron-tunneling setup of a single-walled carbon nanotube (SWNT) which is weakly coupled to source and drain contacts. The contact magnetization may either be parallel or antiparallel as indicated by the arrows. The gate electrode allows to shift the chemical potential inside the SWNT.

From the theoretical point of view, spin-dependent transport in interacting SWNTs has been discussed so far in the limit of very long nanotubes¹⁵, for tubes in the Fabry-Perot regime¹⁶ and for SWNT-based quantum dots¹⁷⁻¹⁹. In the three latter works the characteristic four-electron shell-filling could be observed in the stability diagrams. In¹⁷ however, focus was on medium-to-large diameter SWNTs where exchange effects can be neglected. The studies in^{18,19} are based on the theory by Oreg et al.⁶, where exchange interactions are treated on a mean-field level, and focus predominantly on shot noise¹⁸ and cotunneling¹⁹ effects.

In this work we generalize the previous investigations of Ref.¹⁷ to include the short range Coulomb interactions causing exchange splittings of the six otherwise degenerate (at vanishing orbital mismatch) $4n + 2$ - filling groundstates. The leads are either parallel or antiparallel spin-polarized and weakly coupled to the SWNT, see Fig. 1. In the low bias regime we derive analytical formulas for the conductance for both large and small

orbital mismatch corresponding to an $S = 0$ and $S = \hbar$ groundstate, respectively, at $4n + 2$ filling. In the high bias regime we numerically calculate the stability diagrams for the two possible groundstates. We show several differences in transport between parallel and antiparallel lead magnetization, as e.g. a negative differential conductance (NDC) effect occurring only for the $S = 0$ groundstate and antiparallel magnetization. We further include in the calculations a parallel magnetic field leading to a Zeeman splitting for all states with total spin unequal to zero. It is then possible to observe spin blocking effects due to transport channels that trap the system in the triplet state with $S_z = -\hbar$. Performing a magnetic field sweep, a groundstate change may be obtained as it has been shown experimentally⁸.

The paper is organized as follows. In section II we discuss the relevant features of the low energy Hamiltonian of interacting SWNTs with special focus on the filling $4n + 2$. In section III we describe the set-up and method used to study spin-dependent transport in the sequential tunneling regime. Finally, in section IV, we present our results for the conductance, while in section V we focus on the nonlinear (finite bias) regime.

II. THE INTERACTING LOW ENERGY SPECTRUM

A. The interacting Hamiltonian

The starting point for a microscopic, but still analytical, treatment of SWNTs is a tight-binding ansatz for the wavefunction of the $2p_z$ - electrons on the graphene honeycomb lattice. Including nearest neighbor hopping matrix elements it yields an electron-hole symmetric band-structure with a fully occupied valence band and an empty conduction band. Since the two bands touch at the cornerpoints of the 1st Brillouin zone, the Fermi-points, graphene is a zero gap semiconductor. Wrapping the considered sheet of graphene, i.e., imposing periodic boundary conditions (PBCs) around the circumference, yields a SWNT and leads to the formation of transverse subbands. For the low energy electronic structure of metallic SWNTs, only the subbands touching at the Fermi-points are of relevance. In the following we consider armchair SWNTs of finite length and impose open boundary conditions (OBCs) at the two ends of the tube, i.e., that the wave function vanishes at the armchair edges. This condition mixes the two inequivalent Fermi points $F = \pm K_0$ from the underlying graphene first Brillouin zone and yields the linear dispersion relation of the finite size SWNT shown in Fig. 2. It is characterized by two linear branches $r = \pm$ of slope $\pm \hbar v_F$ with the Fermi velocity $v_F \approx 8.1 \cdot 10^5 \frac{m}{s}$. The allowed quasi-momentum values are given by $\kappa = (n_\kappa + \Delta)\pi/L$, where $n_\kappa \in \mathbb{Z}$, L is the tube length and Δ accounts for the fact that K_0 may not be an integer multiple of π/L . The kinetic part of the Hamiltonian, yielding the energy relative to the

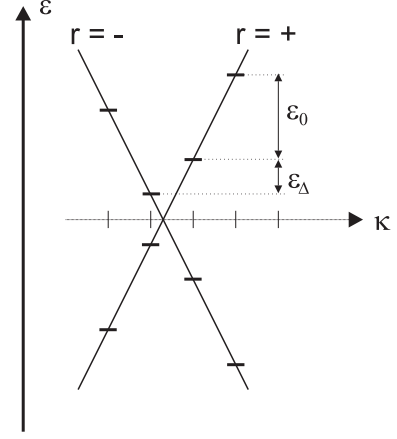


FIG. 2: The dispersion relation of a noninteracting SWNT with open boundary conditions. It is characterized by two linear branches, $r = \pm$, of slope $\pm \hbar v_F$ determined by the Fermi velocity v_F . The quantities ϵ_0 and ϵ_Δ are the intraband level spacing and the orbital mismatch energy, respectively.

Fermi-sea, correspondingly reads

$$H_0 = \epsilon_0 \sum_{r\sigma} r \sum_{n_\kappa} n_\kappa c_{r\sigma\kappa}^\dagger c_{r\sigma\kappa} + \epsilon_\Delta \sum_{r\sigma} r N_{r\sigma}, \quad (1)$$

where $\epsilon_0 = \hbar v_F \pi / L$ is the level spacing, and $\epsilon_\Delta \equiv \epsilon_0 \Delta$ is the band offset energy. Finally $c_{r\sigma\kappa}^\dagger$ creates an electron with momentum κ and spin σ in branch r and the operator $N_{r\sigma}$ counts the total electron number in branch r and of spin σ .

The interaction part of the Hamiltonian is given by

$$V = \frac{1}{2} \sum_{\sigma\sigma'} \iint d^3r d^3r' \Psi_\sigma^\dagger(\vec{r}) \Psi_{\sigma'}^\dagger(\vec{r}') U(\vec{r} - \vec{r}') \Psi_{\sigma'}(\vec{r}') \Psi_\sigma(\vec{r}), \quad (2)$$

where Ψ, Ψ^\dagger are fermion field operators and we use the Ohno-potential²⁰,

$$U(\vec{r} - \vec{r}') = U_0 \left(1 + \left(\frac{U_0 \epsilon |\vec{r} - \vec{r}'|}{14.397} \right)^2 \right)^{-\frac{1}{2}} eV, \quad (3)$$

with $U_0 = 15 \text{ meV}^{21}$ and $\epsilon \simeq 1.4 - 2.4^4$ is the dielectric constant of graphene. In the next step we express the 3D electron operators in terms of the 1D fermion-fields²²

$$\psi_{rF\sigma}(x) = \frac{1}{\sqrt{2L}} \sum_{\kappa} e^{i \text{sgn}(F) \kappa x} c_{r\sigma\kappa}, \quad (4)$$

and obtain

$$\Psi_\sigma(\vec{r}) = \sqrt{L} \sum_{rF} \text{sgn}(F) \psi_{rF\sigma}(x) \sum_p f_{pr} \varphi_{pF}(\vec{r}). \quad (5)$$

Here $F = \pm K_0$ denotes the two independent Fermi-points, $p = \pm$ the two sublattices of graphene, and the

coefficients f_{pr} of the sublattice wave function $\varphi_{pF}(\vec{r})$ are given by $1/\sqrt{2}$ for $p = +$ and $-r/\sqrt{2}$ for $p = -$. The sublattice wave function itself reads

$$\varphi_{pF}(\vec{r}) = \frac{1}{\sqrt{N_L}} \sum_{\vec{R} \in L_G} e^{iF\vec{R}_x} \chi_{p_z}(\vec{r} - \vec{R} - \vec{\tau}_p), \quad (6)$$

where N_L is the number of graphene lattice sites identified by the lattice vector \vec{R} , and L_G denotes the graphene honeycomb lattice in real space. Furthermore, $\chi_{p_z}(\vec{r} - \vec{R} - \vec{\tau}_p)$ is the p_z wavefunction of a carbon atom living on sublattice p , identified by the sublattice vector $\vec{\tau}_p$. Upon integrating Eq. (2) over the coordinates radial to the tube axis, one eventually arrives at a 1D interaction potential characterized by density-density and non density-density contribution⁷ so that the total Hamiltonian reads

$$H_\odot = H_0 + V_{\rho\rho} + V_{n\rho\rho}. \quad (7)$$

With the help of bosonization²⁵ it is possible to diagonalize the density part $H_0 + V_{\rho\rho}$. Eventually the bosonized and diagonalized Hamiltonian takes the form⁷:

$$H_0 + V_{\rho\rho} = \sum_{j\delta q > 0} \epsilon_{j\delta q} a_{j\delta q}^\dagger a_{j\delta q} + \frac{1}{2} E_c N_c^2 + \frac{1}{2} \sum_{r\sigma} N_{r\sigma} \left[-\frac{J}{2} N_{-r\sigma} + (\epsilon_0 - u^+) N_{r\sigma} + r\epsilon_\Delta \right]. \quad (8)$$

Besides the ground state, it accounts for all the possible fermionic and bosonic excitations of a SWNT. The bosonic excitations are described by the first term on the right hand side. The indices refer to total/relative ($\delta = +/ -$) charge/spin ($j = c/s$) modes. The energies $\epsilon_{j\delta q}$ are given by

$$\epsilon_{j\delta q} \cong \begin{cases} \epsilon_0 n_q \sqrt{1 + \frac{8W_q}{\epsilon_0}} & j\delta = c+ \\ \epsilon_0 n_q & j\delta = c-, s+, s- \end{cases}, \quad (9)$$

with $q = n_q \pi / L$ for $n_q \in \mathbb{Z}$ and

$$W_q = \frac{1}{(2L)^2} \int_0^L dx \int_0^L dx' U^{\text{long}}(x, x') \times 4 \cos(qx) \cos(qx'), \quad (10)$$

the contribution of the long-ranged density-density processes. Indeed $U^{\text{long}}(x, x') = [U^{\text{intra}} + U^{\text{inter}}]/2$ is the sum of the interaction potentials for electrons living in the same (intra) and different (sublattices):

$$U^{\text{intra/inter}}(x, x') = L^2 \int \int d^2 r_\perp d^2 r'_\perp \times \varphi_{pF}^*(\vec{r}) \varphi_{\pm pF'}^*(\vec{r}') \varphi_{\pm pF'}(\vec{r}') \varphi_{pF}(\vec{r}) U(\vec{r} - \vec{r}'). \quad (11)$$

The second summand of (8) is the charging term with the charging energy $E_c = W_{q=0}$ and also comes from the long range part of the Coulomb interaction. It counts the energy one has to spend to put $N_c = \sum_{r\sigma} N_{r\sigma}$ electrons on the dot, no matter what spin $\sigma \in \{\uparrow, \downarrow\}$ or pseudospin $r \in \{+, -\}$ they have. The second line of (8) starts with an exchange term favoring spin alignment. The exchange-splitting,

$$J = \frac{1}{2N_L^2} \sum_{\vec{R}, \vec{R}'} (1 + e^{-i2K_0(R_x - R'_x)}) \times [U(\vec{R} - \vec{R}') - U(\vec{R} - \vec{R}' + \vec{\tau}_p - \vec{\tau}_{-p})], \quad (12)$$

being proportional to the difference of the Coulomb interaction for electrons on the same and on different sublattices, accounts for the contribution of short range processes. The next term in (8) reflects the energy cost for adding electrons of the same spin band in the same branch, i.e., the Pauli-principle, where the correction u^+ is

$$u^+ = \frac{1}{4N_L^2} \sum_{\vec{R}, \vec{R}'} e^{-i2K_0(R_x - R'_x)} \times [U(\vec{R} - \vec{R}') + U(\vec{R} - \vec{R}' + \vec{\tau}_p - \vec{\tau}_{-p})]. \quad (13)$$

Finally, the last term accounts for a possible band-mismatch, see Fig. 2.

The eigenstates of $H_0 + V_{\rho\rho}$ are spanned by

$$|\vec{N}, \vec{m}\rangle = \prod_{j\delta q} \frac{(a_{j\delta q}^\dagger)^{m_{j\delta q}}}{\sqrt{m_{j\delta q}!}} |\vec{N}, 0\rangle. \quad (14)$$

Here \vec{N} and \vec{m} denote the fermionic and the bosonic configuration, respectively, such that the state $|\vec{N}, 0\rangle$ has no bosonic excitation. The fermionic configuration is given by the number of electrons in each branch with a certain spin $\vec{N} = (N_{-\uparrow}, N_{-\downarrow}, N_{+\uparrow}, N_{+\downarrow})$. These eigenstates will be used to calculate the contribution of the non-density part of the interaction, i.e., $\langle \vec{N}, \vec{m} | V_{n\rho\rho} | \vec{N}', \vec{m}' \rangle$. Away from half-filling, they only couple states close in energy and one is allowed to work with a truncated eigenbasis (we check convergence of the results as the basis is enlarged). As shown by Yoshioka and Odintsov²³, for long SWNTs a Mott-insulating transition is expected to occur at half-filling due to umklapp scattering. As found in Ref.⁷ umklapp processes acquire increasing weight as half-filling is approached also for finite size tubes, a possible signature of the Mott instability, and the present theory breaks down. In recent experiments²⁴ the observation of the Mott transition in SWNT quantum dots was claimed.

B. Low energy spectrum away from half-filling

The low energy regime is where the energies that can be transferred to the system by the bias voltage and the

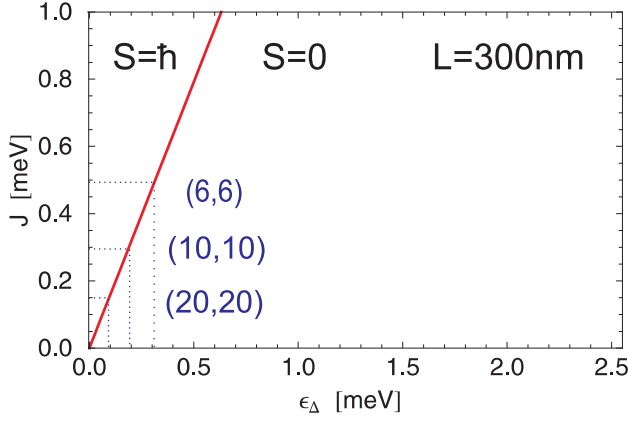


FIG. 4: Phase diagram to determine the groundstate of different tubes of length 300nm. The chance to find a triplet groundstate increases with increasing exchange parameter J , i.e., with decreasing tube diameters.

leads, see Fig. 1, and the main calculation tools. The Hamiltonian of the full system reads

$$H = H_{\odot} + \sum_{l=s,d} H_l + H_T + H_{ext}, \quad (19)$$

where $l = s, d$ denotes the Hamiltonian in the source and the drain contact, respectively. The leads magnetization is accounted for in terms of a Stoner Hamiltonian where the density of states, $\mathcal{D}_{l\sigma}(\epsilon)$, for the majority ($\sigma = \uparrow$) and the minority ($\sigma = \downarrow$) carriers are different. We treat the leads within the wide-band approximation, i.e., we regard the density of states as constant quantities to be evaluated at the leads chemical potentials μ_s and μ_d . We can thus define the polarization by ($l = s, d$):

$$P_l = \frac{\mathcal{D}_{l\uparrow}(\mu_l) - \mathcal{D}_{l\downarrow}(\mu_l)}{\mathcal{D}_{l\uparrow}(\mu_l) + \mathcal{D}_{l\downarrow}(\mu_l)}. \quad (20)$$

Moreover, we will consider a symmetric set up $\mathcal{D}_{s\sigma} = \mathcal{D}_{d\sigma} = \mathcal{D}_{\sigma}$ and $P_s = P_d = P$. The total density of states is given by $\mathcal{D}_{tot} = \mathcal{D}_{\uparrow} + \mathcal{D}_{\downarrow}$. We account for the bias voltage V_b in terms of the difference $eV_b = \mu_s - \mu_d$ between the electrochemical potentials in the source and drain leads. Further, H_T in Eq. (19) is the tunneling Hamiltonian which we will treat as a perturbation since weak coupling to the leads is assumed. Finally, H_{ext} describes the influence of the externally applied gate voltage V_g . The gate is capacitively coupled to the SWNT and hence contributes via a term $e\alpha V_g N_c$ with α a proportionality factor.

In order to evaluate the current-voltage characteristics we use the method developed in Ref.¹⁷ where, starting from the Liouville equation for the density matrix of the full system, a generalized master equation (GME) for the reduced density matrix ρ (RDM) of the SWNT is obtained to second order in H_T . Once the stationary RDM

parameters	label	value
length	L	300.06 nm
diameter	d	0.81 nm
dielectric constant	ϵ	1.4
\Downarrow		
charging energy	E_c	6.7 meV
level spacing	ϵ_0	5.6 meV
Coulomb excess energy	u^+	0.15 meV
exchange energy	J	0.49 meV
orbital mismatch	ϵ_{Δ}	0 meV or 1.68 meV
thermal energy	$k_B T$	4.0×10^{-3} meV
transmission coefficient	$\mathcal{D}_{tot} \Phi$	1×10^{-4} meV

TABLE II: Parameter set of the 300nm (6,6) nanotube investigated in this work.

is known, the stationary current through e.g. the source lead is evaluated from the relation $I_s = eTr\{\rho \hat{N}_s\}$, where N_s is the number operator for electrons in the left lead. As this procedure with the relevant equations is thoroughly explained in Ref.¹⁷, we refrain from repeating it here. The GME can be solved in analytic form in the linear regime, being the focus of the following Sec. IV. In the nonlinear regime, discussed in Sec. V, the differential conductance is evaluated numerically. Moreover, from here on we will focus on the transition between charge states $4n + 1 \longleftrightarrow 4n + 2$, mirror symmetric to $4n + 2 \longleftrightarrow 4n + 3$, as these two transitions are the ones that reveal exchange effects. The remaining transitions $4n \longleftrightarrow 4n + 1$ and $4n + 3 \longleftrightarrow 4(n + 1)$ will not qualitatively change due to the presence of short range processes and we hence refer to the discussion in¹⁷.

If not otherwise specified, we choose nanotubes described by the parameters in table II: In order to obtain an $|a\rangle$ groundstate we assume a band-mismatch of $\epsilon_{\Delta} = 0.3\epsilon_0 = 1.68$ meV, whereas for a triplet groundstate we choose $\epsilon_{\Delta} = 0$.

IV. THE LINEAR REGIME

A. Conductance at zero magnetic field

We focus on the conductance formulas for the two cases of tunneling from the $4n + 1$ groundstates into the $S = 0$ groundstate $|a\rangle$ or into the triplet groundstates.

For the transition $|\sigma, \cdot\rangle \longleftrightarrow |a\rangle$ the conductances in the case of parallel, G^P , and antiparallel, G^{AP} , magnetized leads are found to be

$$G_a^P = \frac{c^2 e^2 \pi}{\hbar} \frac{\gamma}{1 + \gamma} \beta \mathcal{D}_{tot} \Phi \left| \frac{f(\mu_a) f(-\mu_a)}{2 - f(\mu_a)} \right|, \quad (21a)$$

$$G_a^{AP} = \frac{(P^2 - 1) \gamma (1 + \gamma)}{P^2 (\gamma - 1)^2 - (\gamma + 1)^2} G_a^P, \quad (21b)$$

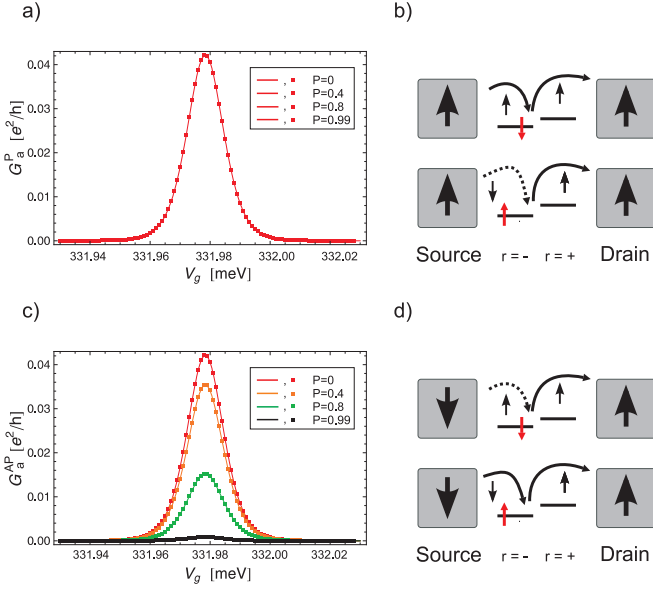


FIG. 5: Panels a) and c). Conductance vs. gate voltage for the $|\sigma, \cdot\rangle \longleftrightarrow |a\rangle$ resonance for parallel, G_a^P , and antiparallel, G_a^{AP} , lead magnetization. In both cases the analytical predictions Eqs. (21a), (21b) (continuous curves) perfectly match with the results from a numerical evaluation of the GME (squares). Strikingly G_a^P is independent of the leads polarization P , while G_a^{AP} is maximal at $P = 0$. Panels b) and d). Schematic explanation of the different polarization dependence. The red spin specifies the spin of the state $|\sigma, \cdot\rangle$. The dashed/continuous arrows indicate rare/favorable tunneling processes. For parallel magnetization, panel b), the fast tunneling channel is the one with an excess spin \downarrow and the electron transferred from source to drain is always a majority electron \uparrow . If the initial dot spin is \uparrow , this is likely to tunnel to the drain, such that at the end of the tunneling process a spin-flip has occurred, leaving the dot in the favorable configuration with a spin \downarrow . For antiparallel lead magnetization, panel d), the fast channel corresponds to one electron in the dot with spin \uparrow . To this channel, however, is associated a spin flip. Because the situation with initial spin \downarrow involves a rare tunneling process from the source lead, the conductance gets diminished by increasing polarization.

with $c = c_1/\sqrt{c_1^2 + 1}$, the Fermi function $f(\mu)$ evaluated at the gate voltage dependent energy difference $\mu_a = E_{|a\rangle} - E_{|\sigma, \cdot\rangle}$ and β the inverse temperature. The parameters $\Phi = \Phi_s$ and $\gamma = \Phi_d/\Phi_s$ describe the possible asymmetric lead transparencies¹⁷ (hereby, Φ is in second order of the tunneling coupling contained in H_T). The conductances are shown in Fig. 5a) and 5c) for the symmetric transparencies case $\gamma = 1$ and $\mathcal{D}_{tot}\Phi = 10^{-4}$ meV. Strikingly, in the parallel magnetized case there is *no* dependence on the polarization since there is never a blocking state involved in transport, see Fig. 5b). For the antiparallel case, in contrast, transport is limited by the weakest channel (when there is a \downarrow -electron on the dot) and one can drive the conductance to zero by tuning the polarization to $P \rightarrow 1$. This feature is explained in Fig. 5d).

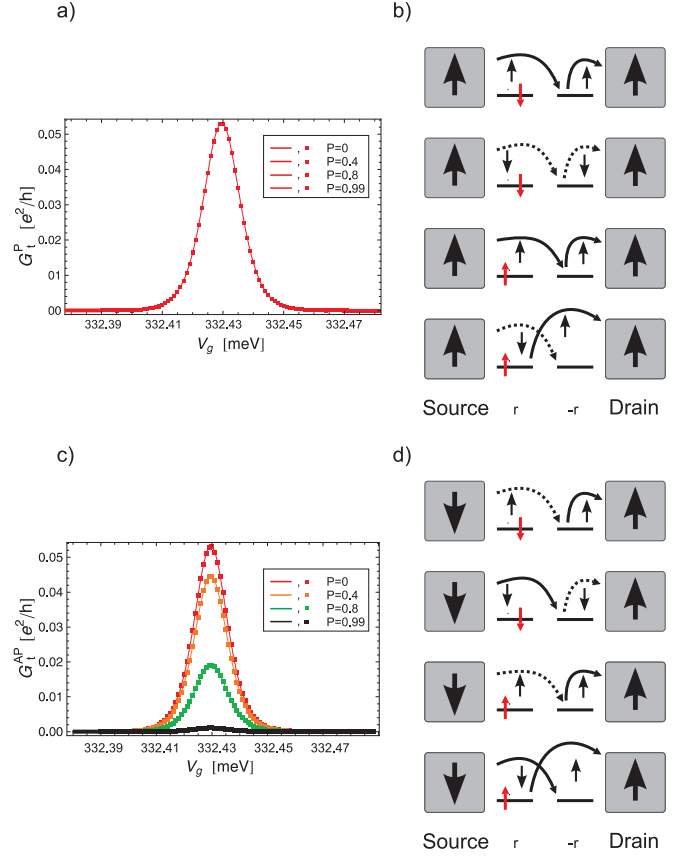


FIG. 6: Panels a) and c). Conductance vs. gate voltage at zero band-mismatch (triplet groundstate) for parallel, G_t^P , and antiparallel, G_t^{AP} , lead magnetization. G_t^P is independent of the leads polarization P , while G_t^{AP} is maximal at $P = 0$. The absolute value of the conductance is slightly larger than for the $|\sigma, \cdot\rangle \longleftrightarrow |a\rangle$ case since more channels are involved. Panels b) and d). Schematic explanation of the different polarization dependence. For simplicity we only drew the case in which the initial excess spin (red spin) is in the $r = +$ branch. For parallel magnetization, panel b), the fast channel corresponds to the $|\uparrow, \cdot\rangle \longleftrightarrow |t_{+1}\rangle$ transition which conserves the spin of the excess dot electron. For antiparallel magnetization, panel d), the fast channel corresponds to an initial excess spin \uparrow electron likely to tunnel to the drain and being replaced by a spin \downarrow from the source. The situation with an initial spin \downarrow , however, corresponds to a weak channel. Increasing the polarization highly populates the $|t_{-1}\rangle$ state and transport decreases.

For the case of the triplet groundstate we face a completely new situation. First, we have for $N_c = 4n + 1$ filling four degenerate states available because the band-mismatch has been chosen to be zero. Secondly, we couple to three different states in the case of $N_c = 4n + 2$ rather than to just one. However, the conductance plots do not qualitatively change as it may be seen in Fig. 6a)

and 6c). The conductance formulas read:

$$G_{1,t}^P = \frac{3e^2\pi}{\hbar} \frac{\gamma}{1+\gamma} \beta \mathcal{D}_{tot} \Phi \left| \frac{f(\mu_t)f(-\mu_t)}{4-f(\mu_t)} \right|, \quad (22a)$$

$$G_{1,t}^{AP} = \frac{(P^2-1)\gamma(1+\gamma)}{P^2(\gamma-1)^2-(\gamma+1)^2} G_{1,t}^P. \quad (22b)$$

Compared to Eqs. (21a), (21b) the prefactor changed from c^2 to 3 due to the three involved triplet states. The quantity $\mu_t = E_{|t\rangle} - E_1$ is the difference between the triplet and the $N_c = 4n+1$ - groundstate energies. In addition, the denominator in the term containing the Fermi-functions has also changed to account for the degeneracy of the $4n+1$ - filling states. The qualitative behavior, however, does not change compared to the case of an $|a\rangle$ groundstate, such that one cannot determine the spin nature of the groundstate from these plots alone.

B. Conductance in the presence of an external magnetic field

In this section we consider the influence of an externally applied magnetic field (Zeeman-field) which clearly reveals the character of the groundstate for $4n+2$ and, moreover, may even change the groundstate depending on the field strength. The field causes an additional Zeeman energy to states with a spin-component $S_z \neq 0$. The sign is negative if the concerned state in the tube is parallel to the external field and positive if antiparallel. Thus, the chemical potential differences appearing in Eqs. (21a), (21b), (22a) and (22b) will be shifted by $\pm E_z = \pm \mu_B B$. We use the convention $\mu_\uparrow = \mu - E_z$ and $\mu_\downarrow = \mu + E_z$. Furthermore, in order to improve the readability, we introduce the abbreviation $f_{\pm\uparrow/\downarrow} = f(\pm\mu_{\uparrow/\downarrow})$. The conductances for the antiparallel set-up are

$$G_a^{AP}(E_z) = \frac{c^2 e^2 \pi}{2\hbar} \beta \mathcal{D}_{tot} \Phi \times \left| \frac{f_{+\uparrow}f_{+\downarrow}(1+P(\gamma+1)+\gamma)f_{-\downarrow}}{f_{+\downarrow}+f_{+\uparrow}f_{-\downarrow}} + \frac{f_{+\uparrow}f_{+\downarrow}(1-P(\gamma-1)+\gamma)f_{-\uparrow}}{f_{+\downarrow}+f_{+\uparrow}f_{-\downarrow}} \right| \quad (23a)$$

and

$$G_t^{AP}(E_z) = \frac{e^2 \pi}{2\hbar} \beta \mathcal{D}_{tot} \Phi \times \left\{ f_{-\uparrow}f_{-\downarrow} \left[(1+\gamma-P(1-\gamma))f_{+\downarrow}(f_{-\downarrow}f_{+\uparrow}+2f_{+\downarrow}f_{-\uparrow}) + (1+\gamma+P(1-\gamma))f_{+\uparrow}(f_{-\uparrow}f_{+\downarrow}+2f_{-\downarrow}f_{+\uparrow}) \right] \right\} / \left\{ f_{-\uparrow}(1+f_{-\downarrow})(f_{-\downarrow}f_{+\uparrow}+f_{-\uparrow}f_{+\downarrow}) + f_{-\downarrow}^2 f_{+\uparrow}^2 \right\}. \quad (23b)$$

We do not find qualitative differences with respect to the zero magnetic field case: the conductances decrease in

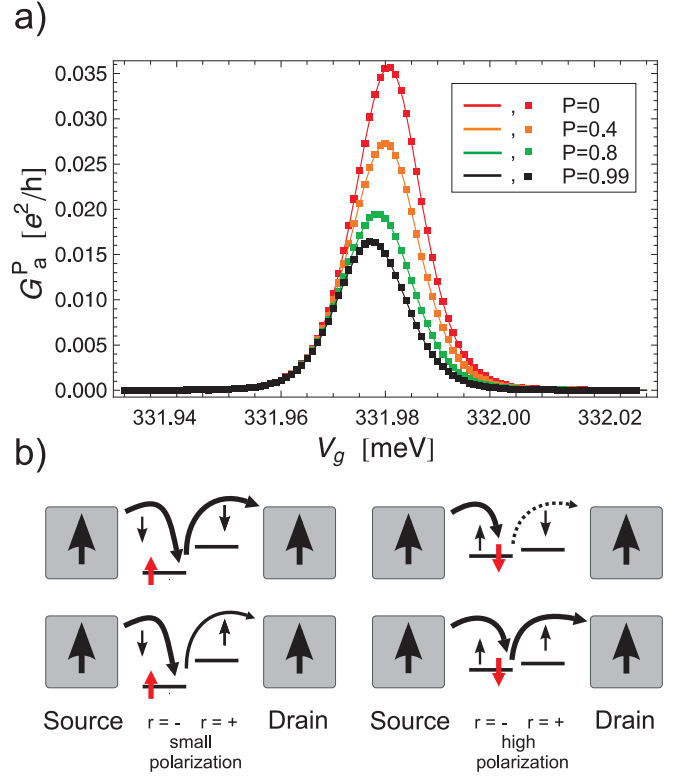


FIG. 7: a) Conductance near the $|\sigma, \cdot\rangle \longleftrightarrow |a\rangle$ transition for parallel magnetized leads and applied magnetic field. The peaks corresponding to higher polarizations are shifted to lower gate voltages. b) Schematic explanation of the polarization and gate-voltage dependence for small (left sketch) and large (right sketch) polarization. The red spin indicates the spin of the excess electron initially present on the dot. The thick and thin lines are frequent and less frequent transitions, while dashed lines indicate rare transitions. Large polarizations favor processes involving majority spins while, due to the extra required Zeeman energy, the Fermi function suppresses processes where a spin \downarrow is transferred. Thus at small polarizations the transport is mostly mediated by spin \downarrow - electrons while at large polarizations \uparrow - electrons are preferred. Correspondingly the peak position is shifted to smaller gate voltages as the polarization is increased.

both cases with increasing polarization. In the following, we will therefore only focus on the parallel case, where we find interesting behavior for small Zeeman splittings. The conductance formulas for parallel lead magnetization take the form

$$G_a^P(E_z) = \frac{c^2 e^2 \pi}{\hbar} \frac{\gamma}{1+\gamma} \beta \mathcal{D}_{tot} \Phi \times \left| \frac{f_{+\uparrow}f_{+\downarrow}[(P+1)f_{-\uparrow}-(P-1)f_{-\downarrow}]}{f_{+\uparrow}f_{+\downarrow}+f_{+\downarrow}f_{-\uparrow}+f_{+\uparrow}f_{-\downarrow}} \right| \quad (24a)$$

and

$$\begin{aligned}
G_t^P(E_z) = & \frac{e^2 \pi}{2\hbar} \frac{\gamma}{1+\gamma} \beta \mathcal{D}_{tot} \Phi \\
& \times \left| \left\{ f_{-\uparrow} f_{-\downarrow} \left[(P+1) f_{+\uparrow} \left(f_{-\uparrow}^2 f_{+\downarrow} \right. \right. \right. \right. \\
& + f_{+\uparrow} f_{-\uparrow} f_{+\downarrow} + 2 f_{+\uparrow} f_{-\uparrow} f_{-\downarrow} + 2 f_{+\uparrow}^2 f_{-\downarrow} \Big) \\
& - (P-1) f_{+\downarrow} \left(f_{-\downarrow}^2 f_{+\uparrow} + 2 f_{+\downarrow}^2 f_{-\uparrow} \right. \\
& + 2 f_{+\downarrow} f_{-\uparrow} f_{-\downarrow} + f_{+\downarrow} f_{+\uparrow} f_{-\downarrow} \Big) \Big] \Big\} / \\
& \left\{ 2 f_{-\downarrow}^2 f_{+\uparrow} f_{-\uparrow} + f_{+\uparrow}^2 f_{-\uparrow}^2 \right. \\
& \left. + f_{-\uparrow}^2 f_{+\downarrow}^2 + 2 f_{-\uparrow}^2 f_{-\downarrow} f_{+\uparrow} + f_{-\downarrow} f_{-\uparrow} f_{+\uparrow} f_{+\downarrow} \right\} \Big|. \quad (24b)
\end{aligned}$$

The corresponding plots can be seen in Figs. 7a) and 8a). In these calculations we considered a small magnetic field of 0.07 T which equals in magnitude the thermal energy of $k_B T = 0.004$ meV. This provides a situation with a finite occupation probability for all included states. Specifically, this means that also states containing \downarrow - electrons will be populated, but the population of states containing \uparrow - electrons will be preferred. The first thing we observe in both Fig. 7a) and 8a) is that the once degenerate curves in Figs. 5a) and 6a) now split into distinct curves for the four different polarizations. Moreover, the peaks of the curves continuously move to higher gate voltages. Finally the conductance *decreases/increases* with increasing polarization for the *a/t* cases, respectively. Let us examine the results starting with the $|a\rangle$ - groundstate. We will divide the analysis in two cases, slightly polarized leads and strongly polarized leads.

For only slightly polarized or non-polarized leads the situation is intricate as we have to deal with *competing processes*. On the one hand there is a highly populated $|\uparrow, \cdot\rangle$ state and a slightly populated $|\downarrow, \cdot\rangle$ state in the tube. From this point of view, the system prefers \downarrow - electrons to tunnel into the $|a\rangle$ state and to leave the dot subsequently such that the tube always remains in the preferred $|\uparrow, \cdot\rangle$ state (Fig. 7, sketch b), upper left panel). Only rarely, the \uparrow - electron tunnels out, as this would result in a spin-flip to the disfavored $|\downarrow, \cdot\rangle$ state (Fig. 7, sketch b), lower left panel). On the other hand, entering of \downarrow - electrons is suppressed compared to transport of \uparrow - electrons, not so much by the small polarization, but mainly due to the Zeeman splitting in the involved Fermi-functions: The chemical potential for \downarrow - electrons exceeds the one for \uparrow - electrons by $2E_z$ such that $f_{+\uparrow} > f_{+\downarrow}$ at any gate voltage. However, in the end it will be a mixture of mainly \downarrow - electrons and some \uparrow - electrons responsible for transport. This can also be seen by the fact that the curves for small polarizations are shifted to higher gate voltages which accounts for the higher chemical potential of the \downarrow - electrons. In addition, the total amplitude of the conductance is decreased compared to the case without the magnetic field, Fig. 5a),

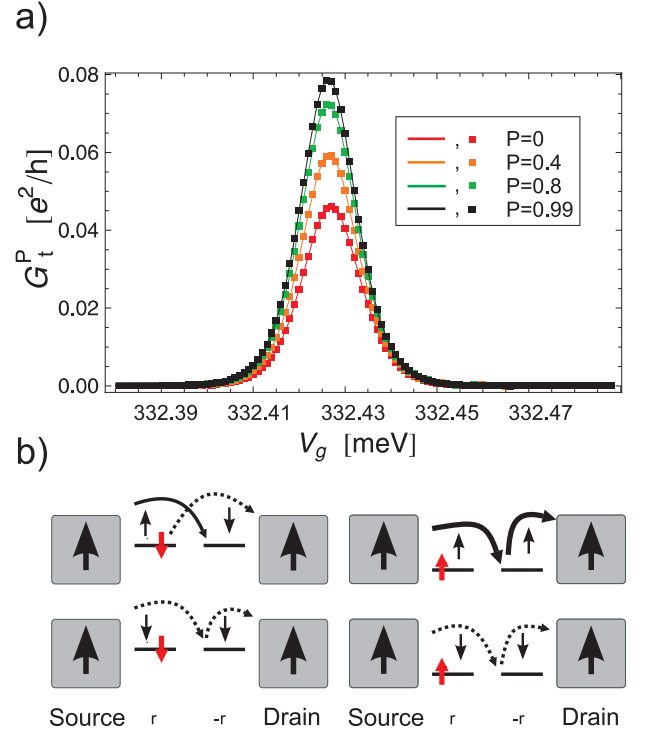


FIG. 8: a) Conductance near the triplet resonance for parallel magnetized leads and applied magnetic field. In contrast to the case of a singlet resonance, Fig. 7, transport increases as the polarization is enhanced. b) Schematic explanation. At small leads polarization the distribution of \uparrow - electrons and \downarrow - electrons is almost equal. However, the $|t_1\rangle$ - channel is preferred to the others. Increasing the polarization enhances the dominance of this channel and correspondingly the conductance. Simultaneously the conductance peak is shifted to lower gate voltage indicating the dominance of \uparrow - electrons.

as there is always a limiting element - either the small Fermi-function or the small population - involved.

In the case of highly polarized leads we face the situation where there are very few \downarrow - electrons in the leads. As temperature provides a small, but nonzero population of the slightly excited state $|\downarrow, \cdot\rangle$, current mainly flows via the polarization-favored \uparrow - electron channel. Since the chemical potential, the increment of the Fermi-functions, is smaller than in the former case the transition takes place at slightly lower gate voltages. The situation again is visualized in the sketch b) of Fig. 7, in the upper and lower right panel.

At the triplet resonance we observe not only quantitative, but also qualitative changes. The plot can be seen in Fig. 8a) and all relevant tunneling processes are sketched in Fig. 8b). Let us again start with unpolarized or just slightly polarized leads. Due to a large population of the spin \uparrow states in the $N_c = 4n + 1$ case and of the $|t_1\rangle$ state in the $N_c = 4n + 2$ case transport is mainly mediated via the majority charge carriers, i.e. \uparrow - electrons (Fig. 8b), upper right panel). However, the resulting current is smaller than in the case without magnetic field since

it is harder to make use of the \downarrow - electrons that are still largely at disposal in the leads.

A high polarization decreases the number of \downarrow - electrons in the leads in favor of the \uparrow - electron number, and such transport via the already preferred $|t_1\rangle$ channel is strongly enhanced. As a consequence, the conductance by far *exceeds* the conductance without magnetic field and polarization. This effect should be detectable in an experimental setup and would give a possibility to distinguish between a triplet groundstate and a $S = 0$ groundstate.

V. THE NONLINEAR REGIME

In the finite bias regime also excited states become available and, due to the resulting high number of involved states, it is necessary to calculate the current numerically. We show the current and the stability diagrams - the differential conductance $\frac{dI}{dV_b}(V_b, V_g)$ as a function of the gate and the bias voltage. The stability diagrams give a clear indication whether the involved groundstate in the transition $4n + 1 \longleftrightarrow 4n + 2$ is the $|a\rangle$ state or the triplet. In the case of antiparallel lead magnetization we find negative differential conductance (NDC) for transitions involving the $|a\rangle$ state. We also observe NDC for transitions involving the $|a\rangle$ state or the triplet if an external magnetic field is applied.

The current as a function of the gate and the bias voltage is shown in Fig. 9a) for the $|a\rangle$ groundstate and in Fig. 9b) for the triplet groundstate. All states with up to one bosonic excitation have been included in the calculation. A 4-electron periodicity of the Coulomb diamonds is clearly seen. The change in color indicates a change in current and therefore the opening of a new channel. At high bias a smearing of the transitions due to the multitude of bosonic excitations is observed. In the remaining of this section we focus on the gate voltage region relevant for the $4n + 1 \longleftrightarrow 4n + 2$ transitions. In the plots of the differential conductance reported in the following we did not include the bosonic excitations to avoid a multitude of transition not relevant for the coming discussion. A polarization $P = 0.9$ is chosen.

A. Differential conductance at zero magnetic field

Figs. 10a) and Fig. 10b) show the stability diagrams for parallel and antiparallel lead magnetization, respectively, for the case of the $|a\rangle$ groundstate. The two transition lines h and e were emphasized by a dashed line because these lines are so weak that it was not possible to resolve them together with the other stronger lines. The most obvious difference between the parallel and the antiparallel setup is the weakness of all transition lines beyond the triplet occupation (line b) for antiparallel lead magnetization. Moreover an NDC line, (line

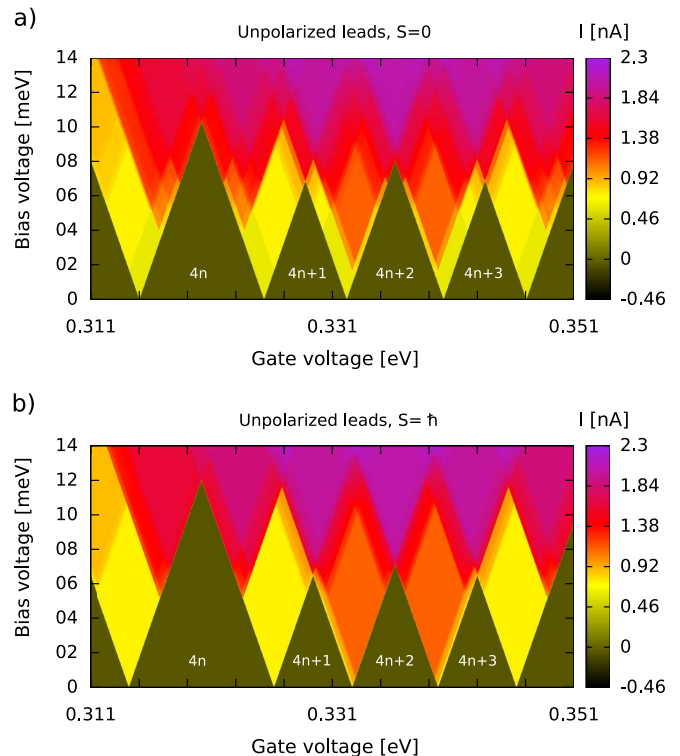


FIG. 9: Current versus gate and bias voltages for unpolarized leads. In total 176 states have been included, which corresponds to all states with at most one bosonic excitation. For $4n + 2$ -filling this amounts to 32 different states. a) Band-mismatch $\epsilon_\Delta = 0.3 \epsilon_0$ corresponding to an $S = 0$ groundstate for the $4n + 2$ filling. b) Band-mismatch $\epsilon_\Delta = 0$ corresponding to an $S = \hbar$ groundstate at filling $4n + 2$. In both cases a 4-electron periodicity of the Coulomb diamonds is observed.

b), not present in the parallel magnetization case, is observed.

In order to explain the line positions in Fig. 10a),b) we provide a schematic drawing in Fig. 11 which is based on a bias trace at the particular gate voltage which aligns the groundstates (white vertical lines in Fig. 10). The differently colored arrows stand for new transport channels that open at certain bias voltages. The channels open in the order of a to e for transitions from $4n + 1 \longrightarrow 4n + 2$ (dashed arrows) and f to h for transitions from $4n + 2 \longrightarrow 4n + 1$ (solid arrows). Sometimes opening of a new channel also opens other channels that have been blocked before and one does not see distinct lines for these transitions. Fig. 11 relates the concerned transitions to the required bias voltages. Moreover, the line g stands for transitions between the triplet and the $|\cdot, \sigma\rangle$ states, i.e., it is a transition between excited states.

To explain the NDC in Fig. 10b) which follows upon line b in the range between lines f and line g , we observe that –in correspondence of the b line– below the resonance only the transitions from $|\sigma, \cdot\rangle$ to the $|a\rangle$ state is possible. Above resonance also the triplet $|t\rangle$ is accessible. For the case of antiparallel polarization, both

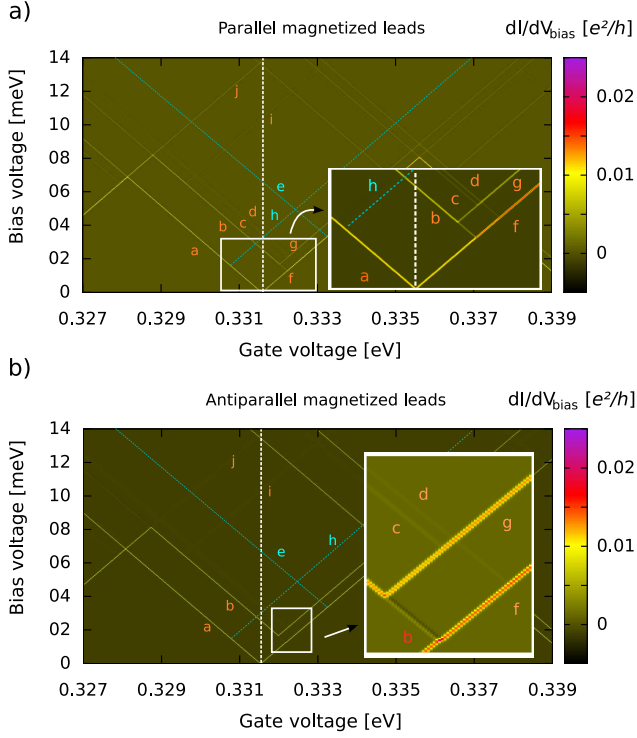


FIG. 10: Differential conductance for transitions between $4n+1 \longleftrightarrow 4n+2$ filling in the $|a\rangle$ - groundstate. The polarization has been chosen to be $P = 0.9$. The four lowest lying states for $4n+1$ and the six ones for $4n+2$ filling were included. The vertical white line is the bias trace we follow to explain the distinct transition lines in Fig. 11. a) The leads are magnetized in parallel. b) Antiparallel magnetized leads. We observe a different intensity of the excitation lines between parallel and antiparallel magnetization. In particular a pronounced negative differential conductance (NDC) occurs in correspondence of the transition between $|\sigma, \cdot\rangle$ and the triplet (line b).

provide only weak transport channels: below the resonance transport is mostly mediated by \uparrow - electrons (see also sketch of Fig. 5) which are minority electrons for the source contact; above resonance, after some tunneling processes the system will always end up in the $|t_{-1}\rangle$ state which is a trapping state. Just at the exact resonance, the thermal energy allows electrons to tunnel forth and back, i.e., a \downarrow - electron has the possibility to tunnel back into the source contact and transport is slightly enhanced. Once the bias voltage exceeds the exact resonance the trapping state $|t_{-1}\rangle$ gets occupied for long times and the current diminishes again.

The fact that the $|\downarrow, \cdot\rangle \longleftrightarrow |t_{-1}\rangle$ transition serves as the major transport channel once it has been opened is also the reason why all transition lines above line b are so weak.

In Figs. 12a) and 12b) the stability diagrams for the $S = \hbar$ triplet groundstate are shown. They look a lot simpler than the ones in Fig. 10 due to the absence of a band-mismatch, causing a degeneracy of all four $4n+1$

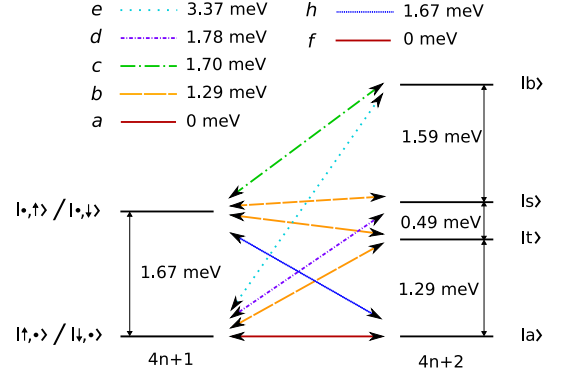


FIG. 11: Schematic drawing for the possible transitions occurring by sweeping the bias voltage at the gate voltage that aligns the $|\sigma, \cdot\rangle$ and the $|a\rangle$ -states (white dashed line in Fig. 10).

filling groundstates. Line a is the groundstate to groundstate transition. Lines b to d indicate transitions from the $4n+1$ groundstates to $|a\rangle$, $|s\rangle$ and $|b\rangle$, respectively. They come in the expected order, at an applied voltage $V_b/2$ equal to u^+ , J and $J+u^+$, as it is shown in table I. Line e stands for the transition from the triplet to one of the $4n+1$ groundstates.

For the antiparallel setup, Fig. 12b), we may see the same effect as we have observed in Fig. 10b), i.e., all lines beyond the transition to the triplet decrease in intensity. Since the triplet is the groundstate, this means all excitation lines are weak and may not be resolved in the figure.

B. Differential conductance in parallel magnetic field

Here we present results for an applied magnetic field of strength $E_z = 0.1$ meV, Fig. 13. The leads are parallel magnetized and a polarization of $P = 0.6$ has been applied. The magnetic field removes the spin degeneracy of the triplet as well as of the $4n+1$ filled states; the resulting Zeeman split transitions are clearly seen in Fig. 13 a) and are less well resolved in Fig. 13 b).

Explicitly, for the $|a\rangle$ groundstate, line b from Fig. 10 splits into lines b and c in Fig. 13. We notice that line c shows an NDC effect due to the opening of the channel $|\downarrow, \cdot\rangle \rightarrow |t_{-1}\rangle$: though this transition, as mediated by minority \downarrow - electrons, is rare, once it happens the system is trapped in the $|t_{-1}\rangle$ state for a long time due to the parallel polarization of the leads. For transitions from $4n+2$ to $4n+1$ line k is a new line that was Coulomb blocked in Fig. 10. It denotes the transition $|s\rangle \rightarrow |\cdot, \downarrow\rangle$ and ends in line e since the $|s\rangle$ state must be populated. Also, we notice the absence of the $|s\rangle \rightarrow |\uparrow, \cdot\rangle$ line since it is Coulomb blocked by the groundstate to groundstate transition (line j).

For the $S = \hbar$ triplet groundstate, Fig. 13b), we ob-

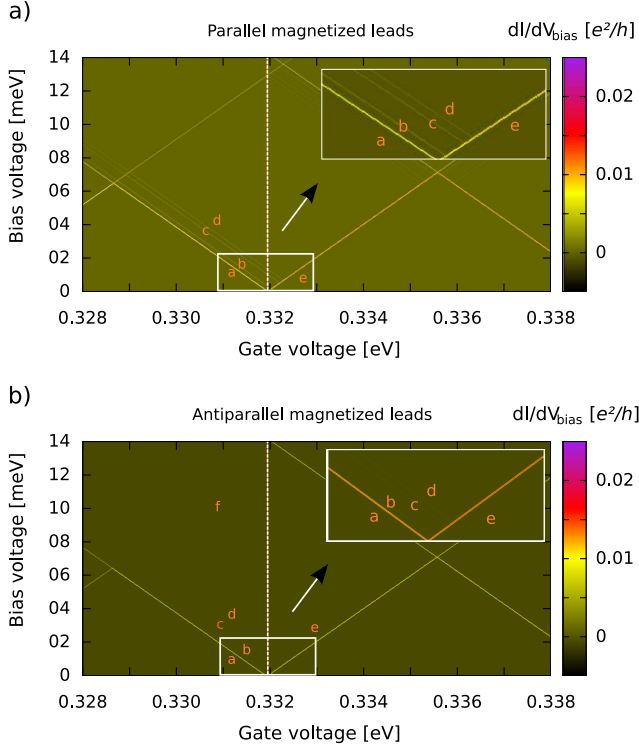


FIG. 12: Differential conductance for transitions between $4n+1 \longleftrightarrow 4n+2$ filling in the triplet groundstate. The polarization has been chosen to be $P=0.9$. The four lowest lying states were included for $4n+1$ and the six lowest ones for $4n+2$. a) Leads parallel magnetized. b) Leads polarized antiparallel. From the stability diagrams it is possible to directly extract the exchange parameters u^+ and J since the bias voltage $V_b/2 = u^+$ is needed to open transition line b and $V_b/2 = J$ to open line c .

serve that line b and line c show NDC effects. Line b represents transitions from $|\cdot, \uparrow\rangle \rightarrow |t_0\rangle$ or $|\uparrow, \cdot\rangle \rightarrow |t_0\rangle$, which is not a trapping state. However, the applied bias voltage is sufficient to also populate the $|\cdot, \downarrow\rangle$ and $|\downarrow, \cdot\rangle$ states from $|t_0\rangle$ and subsequently from $|\cdot, \downarrow\rangle$ and $|\downarrow, \cdot\rangle$ the trapping state $|t_{-1}\rangle$. This process is also visualized in Fig. 14. In the very same way it is possible to get trapped in the $|t_{-1}\rangle$ state via the $|a\rangle$ state indicated by line c .

C. The magnetic field sweep

In a seminal experiment Moriyama et al.⁸ demonstrated a transition from a $S=0$ groundstate to a $S_z = \hbar$ groundstate upon magnetic field sweep in a SWNT quantum dot. In this section we have computed the differential conductance in a gate-voltage and magnetic field plot both for unpolarized, as in⁸, and parallel polarized leads with $P=0.9$.

We start from the $|a\rangle$ groundstate at $B=0$ with a band-mismatch of $0.24 \epsilon_0$ (smaller than we previously used). This choice yields a change of groundstate from

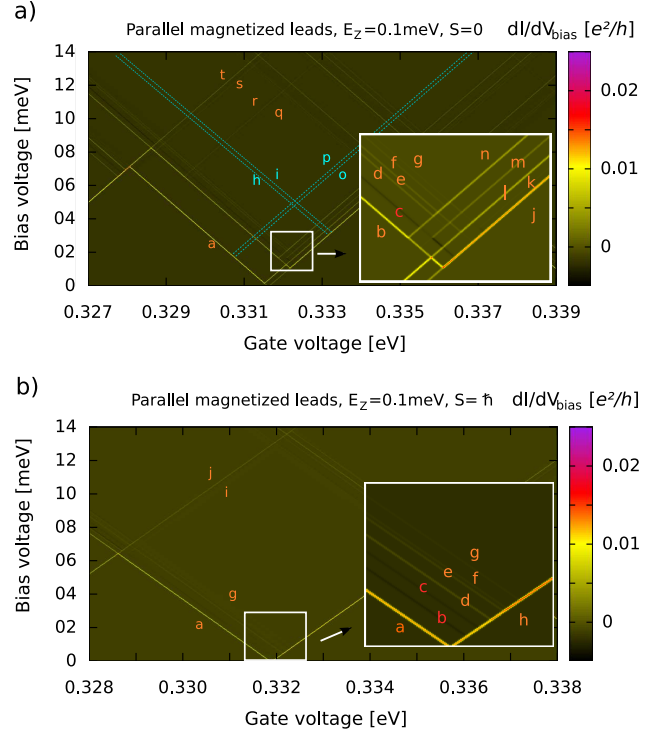


FIG. 13: Differential conductance for transitions between $4n+1 \longleftrightarrow 4n+2$ filling with an applied magnetic field of $E_z = 0.1$ meV. A parallel lead magnetization was assumed with the polarization $P=0.6$. a) $|a\rangle$ - groundstate. Soon after line c an NDC effect is observed due to the occupation of the $|t_{-1}\rangle$ trapping state. b) Triplet groundstate. After lines b and c NDC occurs due to an increased population of the $|t_{-1}\rangle$ state.

$|a\rangle$ to the triplet at a magnetic field $\simeq 6$ T as measured experimentally⁸. To observe well visible patterns, we increased the temperature by a factor of ten compared to Tab. II.

The result of our calculation is presented in Fig. 15a). At a gate voltage of approximately 0.322 meV and 0.323 meV we have two V-shaped transition patterns (a and b) each of width $2E_z = 2\mu_B B$. The separation between a and b at zero field is the band-mismatch ϵ_Δ . Interestingly, for polarized leads, the branches belonging to transitions involving $(|\downarrow, \cdot\rangle, |\cdot, \downarrow\rangle)$, corresponding to the positive slope of the "V", are NDC lines, Fig. 15b). The reason is the same as addressed already in section VB: once the \downarrow - channel becomes available, there is some chance that from time to time a minority charge carrier (\downarrow - electron) enters from the source. As the drain is polarized in parallel to the source, it will take quite a while until this electron can leave the SWNT again, such that transport gets hindered. At the gate voltage of approximately 0.328 meV, one enters the $N_c = 4n+1$ Coulomb diamond (line c) and transport gets completely suppressed. The dot is in the groundstate $|\uparrow, \cdot\rangle$ at $B \neq 0$. At $V_g \simeq 0.329$ meV transport from $N_c = 4n+1$ to the $|a\rangle$ state is enabled (line d).

The next transitions (patterns e, f, g) we observe are

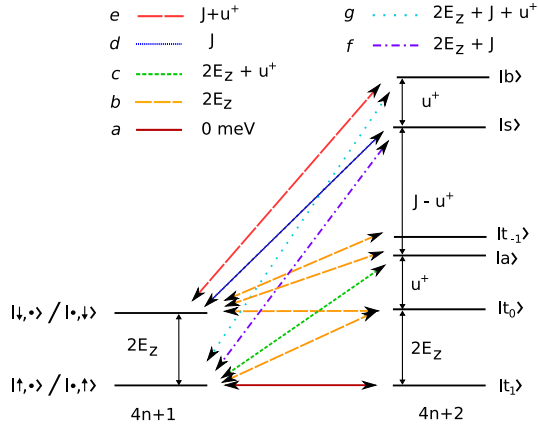


FIG. 14: Schematic drawing of the possible transitions if the $|\cdot, \uparrow\rangle$ and $|\uparrow, \cdot\rangle$ states are aligned to the $|t_1\rangle$ state by the gate voltage at finite magnetic field and in the triplet groundstate. It provides the explanation for the transitions lines observed in the inset of Fig. 13b).

again split by $2E_z$ and therefore shaped like a "V". In all cases, the positively sloped branches are now again of NDC nature for a parallel lead polarization. The first "V" belongs to the triplet (pattern *e*) and is of stronger intensity than the following two patterns. The transitions $|\uparrow, \cdot\rangle \longleftrightarrow |t_1\rangle$ and $|\downarrow, \cdot\rangle \longleftrightarrow |t_0\rangle$ contribute to the negative sloped part, while $|\uparrow, \cdot\rangle \longleftrightarrow |t_0\rangle$ and $|\downarrow, \cdot\rangle \longleftrightarrow |t_{-1}\rangle$ are responsible for the positive shaped line. The crossing of the *e* and *d* lines occurring at $B \cong 6$ T, point *P*, indicates the change in the groundstate from $|a\rangle$ to the state $|t_1\rangle$.

From the triplet pattern *e* the additional gate voltage equal to the exchange energy J is needed to arrive at the last two "V" - shaped patterns *f* and *g*. Compared to the lines for the triplet transition they are quite close to each other and of less intensity. These lines belong to a transition from both the $|\downarrow, \cdot\rangle$ and the $|\uparrow, \cdot\rangle$ states to the $|s\rangle$ - singlet (pattern *f*) and the $|b\rangle$ state (pattern *g*). Finally, the lines on the right edges of the plots are mirror images and belong to backward transitions from $N_c = 4n + 2$ to $N_c = 4n + 1$; for this reason they mark a decrease of current for both polarized and unpolarized leads.

VI. CONCLUSIONS

In summary, we have calculated spin dependent transport through fully interacting SWNTs in both the linear and the nonlinear regime, with and without an applied magnetic field.

Peculiar of metallic SWNTs of small diameter is the possibility, due to exchange interactions, to find the system at $4n + 2$ filling either in a groundstate of total spin $S = 0$ or $S = \hbar$. Which of the two groundstates occurs in a real nanotube depends on the relation between the exchange energy and the orbital band mismatch. Thus,

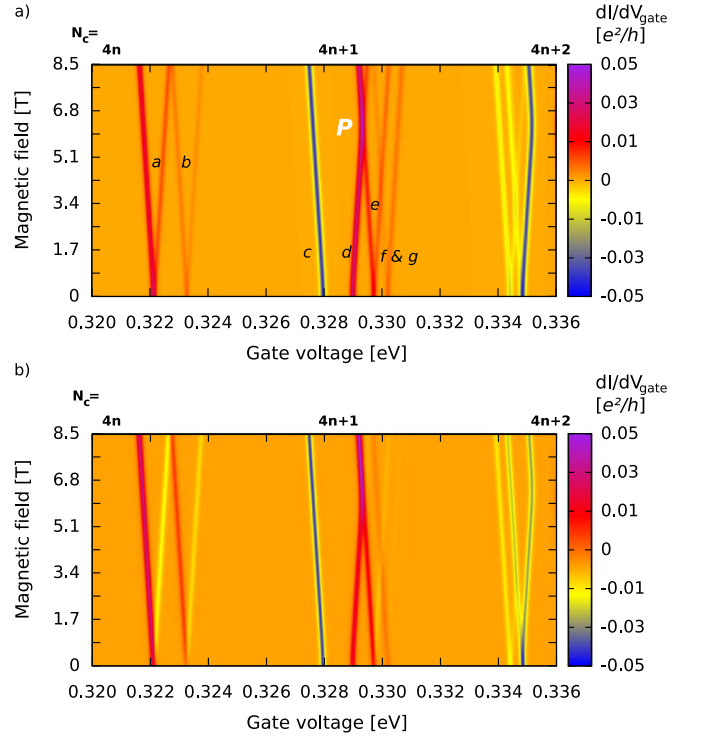


FIG. 15: a) Differential conductance dI/dV_g for a B -field sweep in the $|a\rangle$ - groundstate case. The applied bias voltage was fixed at 5.8 meV. Red lines indicate transitions that become possible at a certain gate voltage and blue lines show a transition that drops out of the transport window. The "V"-shaped patterns *a* and *b* represent transitions from $N_c = 4n$ to $|\sigma, \cdot\rangle$ and $|\cdot, \sigma\rangle$, respectively. Each of the patterns is split by $2E_z$ denoting \uparrow - electrons and \downarrow - electrons tunneling in. At line *c* we enter the $N_c = 4n + 1$ Coulomb diamond and transport gets suppressed. Line *d* stands for the groundstate to groundstate transition from $|\uparrow, \cdot\rangle$ to the $|a\rangle$ - state. The "V"-shaped pattern *e* is due to the transition $N_c = 4n + 1$ to the triplet whereas *f* and *g* denote transitions to the $|s\rangle$ - singlet and the $|b\rangle$ state, respectively. At the point *P* the groundstate changes from the $|a\rangle$ state to the $|t_1\rangle$ - triplet. b) Ferromagnetic leads, polarized in parallel with $P = 0.9$, are assumed. This changes the intensity of the transitions, while their positions are preserved. Moreover, transitions to excited states involving spin-down electrons are disfavored channels and hence converted from positive to negative differential conductance lines.

with focus on transitions involving $4n + 1 \longleftrightarrow 4n + 2$ filling, we investigated both situations and demonstrated pronounced differences in the current-voltage characteristics depending on the considered groundstate. For example in the linear regime the conductance for parallel lead magnetization and finite magnetic field increases by raising the polarization for the case of a triplet groundstate but it decreases for the $S = 0$ groundstate. This is due to the fact that for the triplet groundstate transport is dominated by a channel involving the triplet state $|t_1\rangle$ (with both spins \uparrow); for the $S = 0$ case transport to be mediated by the majority electrons requires

to make use of the $4n + 1$ lowest excited state $|\downarrow, \cdot\rangle$ (and hence less favorable), Zeeman split from the ground state.

In the nonlinear regime we presented stability diagrams with parallel and antiparallel lead magnetization for both ground states. In the antiparallel case it was possible to observe a negative differential conductance (NDC) effect for the $S = 0$ groundstate, following immediately upon a conductance enhancement at the opening of a trapping channel to the excited triplet state $|t_{-1}\rangle$. Directly at that resonance, electrons can, just by thermal activation, tunnel back *and* fourth, such that trapping in the $|t_{-1}\rangle$ state can not yet act, leading to an intermediate conductance increase. Away from resonance, the blocking effect fully occurs, resulting in the NDC. By adding an external magnetic field in the parallel setup we found NDC effects for both groundstates caused by spin blocking mediated by \downarrow - channels, involving in particular the triplet state $|t_{-1}\rangle$.

Finally, we also presented results for the differential conductance in a gate-voltage and magnetic field map at finite bias. These magnetic field sweeps immediately allow to recognize the nature of the $4n + 2$ -filling groundstate at zero field, as well as to tune the nature of the groundstate from $S = 0$ to $S_z = \hbar$ upon variation in the

field amplitude. Our results for unpolarized leads are in *quantitative* agreement with experiments on a small-diameter SWNT by Moryama et al.⁸. Importantly the sweep at zero field also allows to immediately read off the values of the short range interactions J and u^+ . Specifically, J is the singlet-triplet exchange splitting and u^+ characterizes at zero orbital mismatch the energy difference between two of the low energy states of total spin $S = 0$. In the presence of polarized leads the magnetic field sweep also reveals lines of NDC due to the trapping nature of all \downarrow - channels.

The predictions of our theory are in quantitative agreement with experimental results obtained so far for unpolarized leads⁸⁻¹⁰. Due to recent achievements on spin-polarized transport in SWNTs¹²⁻¹⁴, our predictions on spin-dependent transport are within the reach of present experiments.

VII. ACKNOWLEDGMENTS

We acknowledge support by the DFG under the funding programs SFB 689, GRK 638.

-
- ¹ S. Iijima and T. Ichihashi, *Nature* **363**, 603 (1993).
 - ² R. Saito, G. Dresselhaus and M. Dresselhaus, *Physical Properties of Carbon Nanotubes*, (Imperial College Press, London 1998).
 - ³ A. Loiseau *et al.*, *Understanding Carbon Nanotubes*, Lecture Notes in Physics, (Springer, Berlin 2006).
 - ⁴ R. Egger and A.O. Gogolin, *Phys. Rev. Lett.* **79**, 5082 (1997).
 - ⁵ A. A. Odintsov and H. Yoshioka, *Phys. Rev. B* **59**, R10457 (1999).
 - ⁶ Y. Oreg, K. Byczuk and B. I. Halperin, *Phys. Rev. Lett.* **85**, 365 (2000).
 - ⁷ L. Mayrhofer and M. Grifoni, *Eur. Phys. J. B* **63**, 43 (2008).
 - ⁸ S. Moriyama, T. Fuse, M. Suzuki, Y. Aoyagi and K. Ishibashi, *Phys. Rev. Lett.* **94**, 186806 (2005).
 - ⁹ S. Sapmaz *et al.*, *Phys. Rev. B* **71**, 153402 (2005).
 - ¹⁰ W. Liang, M. Bockrath and H. Park, *Phys. Rev. Lett.* **88**, 126801 (2002).
 - ¹¹ A. Cottet *et al.*, *Semicond. Sci. Technol.* **21**, S78 (2006).
 - ¹² S. Sahoo *et al.*, *Nat. Phys.* **1**, 99 (2005).
 - ¹³ H. T. Man, I. J. W. Wever and A. F. Morpurgo *Phys. Rev. B* **73**, 241401(R) (2006).
 - ¹⁴ J.R. Hauptmann, J. Paaske and P. E. Lindelof, *Nat. Phys.* **4**, 373 (2008).
 - ¹⁵ L. Balents and R. Egger, *Phys. Rev. Lett.* **85**, 3464 (2000).
 - ¹⁶ C. S. Pea, L. Balents and K. J. Wiese *Phys. Rev. B* **68**, 205423 (2003).
 - ¹⁷ S. Koller, L. Mayrhofer and M. Grifoni, *New J. Phys.* **9**, 348 (2007).
 - ¹⁸ I. Weymann, J. Barnas and S. Krompievski, *Phys. Rev. B* **76**, 155408 (2007).
 - ¹⁹ I. Weymann, J. Barnas and S. Krompievski, *Phys. Rev. B* **78**, 035422 (2008).
 - ²⁰ W. Barford, *Electronic and Optical Properties of Conjugated Polymers*, (Clarendon Press, Oxford 2005).
 - ²¹ P. Fulde, *Electron Correlations in Molecules and Solids*, (Springer, Berlin-New York 1995).
 - ²² L. Mayrhofer and M. Grifoni, *Eur. Phys. J. B* **56**, 107 (2007).
 - ²³ H. Yoshioka and A.A. Odintsov, *Phys. Rev. Lett.* **82**, 374 (1999).
 - ²⁴ V. V. Deshpande *et al.*, *Science* **323**, 106 (2009).
 - ²⁵ J. v. Delft and H. Schoeller, *Ann. Phys.* **7**, 225 (1998).